Journal of Materials Chemistry A

ROYAL SOCIETY OF CHEMISTRY

PAPER

View Article Online
View Journal | View Issue

Cite this: J. Mater. Chem. A, 2026, 14, 9277

Unraveling the interfacial degradation mechanism of a metal oxide electrocatalyst/gas diffusion layer in Zn–air batteries through FIB-SEM analysis

M. García-Rodríguez, [a] L. González-Souto,[b] J. Hernández-Saz,[c] J. Juan-Juan,[d] J. J. Calvino,[b] D. Cazorla-Amorós [e] and E. Morallón *[a]

Focused Ion Beam-Scanning Electron Microscopy (FIB-SEM) was employed to investigate the Gas Diffusion Layer (GDL), electrocatalyst, and electrolyte interface in rechargeable Zn–Air Batteries (ZABs) using Fresh and Used samples (before and after long-term electrocatalytic activity, respectively). The electrocatalyst was based on (hydro-)oxides of manganese, cobalt and lanthanum and carbon material. The results reveal a loss of material compaction in the Used sample, accompanied by the formation of pores and irregular gaps, as well as enhanced permeation of the electrocatalyst through the GDL, as evidenced in the tomogram. Interestingly, the analysis of the distribution of elements in the Used sample shows important differences, strongly dependent on their chemical properties in the electrolyte used. Mn and Co, the more electroactive elements for the oxygen-involved reactions, remain in proximity to the electrolyte interface, while La forms a preferential region more distant from and parallel to the electrolyte. XPS results indicate that the formation of this region is associated with the generation of lanthanum acetate species, which are responsible for the decrease in conductivity of the Used sample, as demonstrated by electrochemical impedance spectroscopy experiments, in addition to impairing O_2 diffusion along the GDL. Furthermore, DFT calculations support that the formation of lanthanum acetate species from the metal (hydro)oxides is energetically favorable in the presence of zinc acetate electrolyte in ZABs.

Received 10th December 2025
Accepted 13th January 2026

DOI: 10.1039/d5ta10107g

rsc.li/materials-a

1. Introduction

The search for sustainable and high-performance energy storage solutions has brought rechargeable Zn–Air Batteries (ZABs) to the forefront of research due to their high theoretical energy density (1084 Wh kg^{-1}),[1] environmental friendliness, and cost-effectiveness.[2–5] ZABs have emerged as promising candidates for next-generation energy storage systems, particularly for applications requiring long cycle life and high energy output. However, their practical implementation is significantly hampered by various stability issues associated with the anode, electrolyte, and cathode materials.

Zinc is widely used as the anode in Zn-based batteries due to its abundance, low cost, and good reversibility in aqueous electrolytes.[6] However, its application is hindered by dendrite formation during charge–discharge cycles, leading to short circuits and reduced battery lifespan.[7] Additionally, zinc corrosion in alkaline electrolytes generates passive zinc oxide layers and hydrogen gas, which decrease efficiency and compromise safety.[8,9] Moreover, ZAB electrolytes face stability issues. Aqueous electrolytes tend to evaporate and react with CO_2, forming insoluble carbonates (*e.g.*, K_2CO_3 and $KHCO_3$) that obstruct air diffusion in the cathode, leading to capacity degradation.[10–12]

The positive electrode (cathode during the discharge), particularly when employing metal oxides, also presents significant stability concerns. Metal oxides are very promising electrocatalysts for their excellent catalytic activity and structural flexibility, making them suitable for facilitating both the oxygen reduction reaction (ORR) and oxygen evolution reaction (OER).[13–17] However, despite their advantages, metal oxides are susceptible to degradation under operation conditions, which compromises their catalytic efficiency and durability. The degradation mechanisms often involve the formation of undesirable phases, surface passivation, and structural disintegration. The morphology of a cathode is extremely important to its

[a]Universidad de Alicante, Dept. Química Física e Instituto Universitario de Materiales, Ap. 99, E-03080, Alicante, Spain. E-mail: morallon@ua.es
[b]Departamento de Ciencia de los Materiales e Ingeniería Metalúrgica y Química Inorgánica, Universidad de Cádiz, Escuela Superior de Ingeniería, Campus Río San Pedro, Puerto Real, Cádiz 11519, Spain
[c]Departamento de Ingeniería y Ciencia de los Materiales y del Transporte, Universidad de Sevilla, Sevilla, Spain
[d]Servicios Técnicos de Investigación, Universidad de Alicante, Ap. 99, Alicante E-03080, Spain
[e]Universidad de Alicante, Dept. Química Inorgánica e Instituto Universitario de Materiales, Ap. 99, E-03080, Alicante, Spain

electrochemical performance and, to achieve high performance, cathode morphology optimization is required at length scales ranging from the submicron primary particle(s) to the hundreds of microns thick electrode composite.[18] A significant number of studies have focused on the study of surface reconstruction in metal oxides, which is the main cause of the degradation of ZAB performance.[19–21] However, not only is it important to understand the changes in the intrinsic physical and chemical properties of the metal oxides during their use, but also, since these metal oxides are loaded on a gas diffusion layer (GDL), it is essential to unveil the interaction between the electrocatalyst and the GDL.

The GDL plays a vital role in managing the distribution of reactant gases and the removal of reaction products, thereby influencing the electrochemical performance and stability of the cathode.[22] Metal oxide-GDL interaction also determines the redistribution of catalytic species during their use and, consequently, the efficiency of gas diffusion, the effectiveness of the catalytic sites, and the overall durability of the cathode. To elucidate these interactions, we propose the application of the Focused Ion Beam-Scanning Electron Microscopy (FIB-SEM) technique in ZABs. FIB-SEM combines the capabilities of focused ion beam milling for the precise obtention of cross-sectional images using SEM. It allows for high-resolution, three-dimensional imaging of the cathode structure, enabling detailed analysis of the interface between the cathode material and the GDL.[23,24] This technique can reveal microstructural changes, phase and element distributions, and potential degradation pathways at the nanoscale, providing critical insights into the factors affecting cathode stability. The FIB-SEM technique has been mainly applied for (i) cathode materials in Lithium-Ion Batteries (LIBs),[25–28] (ii) Zn anode dendrite formation studies in ZABs[29–31] and (iii) the modeling of the electrolyte and binder distribution in ZAB-GDLs.[32] However, to the best of our knowledge, this technique has not yet been employed to investigate cathode degradation in ZABs.

Therefore, this work delves into the study of the interaction between metal oxide-based cathode materials and the GDL, aiming to elucidate the underlying mechanisms that govern cathode stability in ZABs. Exploring the interfacial region and material interactions through advanced characterization techniques such as FIB-SEM, provides a comprehensive understanding that could pave the way for the development of more robust and efficient ZABs. For this purpose, a ZAB positive electrode (cathode) composed of La, Mn and Co metal oxides mixed with carbon material will be used, due to its high electrochemical performance and stability reported in our previous work.[33] To further investigate the electrocatalytic properties of the material, DFT calculations are performed in order to study the effects of the existing metal species before and after the ZAB stability test.

2. Experimental

2.1. Materials and reagents

The reagents used in this work included Vulcan XC-72R carbon black (Vulcan) from Cabot Corporation, potassium hydroxide (KOH) from VWR Chemicals (99.8% purity), ethanol (C_2H_5OH) from Alfa Aesar (99.5% purity), isopropanol from Acros Organics (99.5% purity), Nafion® 5% w/w, lanthanum(III) nitrate hexahydrate ($La(NO_3)_3 \cdot 6H_2O$) from Sigma Aldrich (99.9% purity), manganese(II) nitrate tetrahydrate ($Mn(NO_3)_2 \cdot 4H_2O$) from Alfa Aesar (98% purity), cobalt(II) nitrate hexahydrate ($Co(NO_3)_2 \cdot 6H_2O$) from Sigma Aldrich (99.9% purity), and hexadecyltrimethylammonium bromide (CTAB) ($CH_3(CH_2)_{15}N(Br)(CH_3)_3$) from Sigma Aldrich (99.9% purity). Additionally, Zn foil from ThermoScientific was used with a purity of 99.98%, and zinc acetate dihydrate ($Zn(O_2CCH_3)_2 \cdot 2H_2O$) from Sigma Aldrich with a purity of 98%. Commercial 20 wt% Pt/C (Sigma-Aldrich, 98% purity) and RuO_2 (ThermoScientific, 99.95% purity, sub-micron powder, surface area 45–65 $m^2\ g^{-1}$) were also utilized for comparison purposes. All solutions were prepared using ultrapure water (18 MΩ cm, Millipore® Milli-Q® water). The gases used, N_2 (99.999%), O_2 (99.995%), and H_2 (99.999%), were provided by Carburos Metálicos and were used without any pretreatment.

2.2. Synthesis procedure

The synthesis procedure was previously published.[33] First, 6 mmol of each metal precursor are mixed in 30 ml of ultrapure water (Co is always introduced at 30% of the Mn amount), and the surfactant CTAB is added in a 1 : 50 ratio with respect to the total metal content. Metal hydroxides are formed by adding drops of 6 M KOH to the solution until a pH ≈ 14 is reached, and then the solution is stirred for 18 h to ensure proper hydroxide formation. The solution is transferred to an autoclave, which is heated in an oven at 180 °C for 48 h. Subsequently, the autoclave is cooled in an ice bath. Then, the material is washed, filtered, and dried at 100 °C. Finally, the sample is calcined at 200 °C for 6 h in air. This calcination temperature is sufficient for complete removal of organic components (aliphatic chains and trimethylammonium groups from the CTAB surfactant) through volatilization, as confirmed by the absence of nitrogen species in the XPS analysis of the final products. The 6-hour duration at 200 °C in air ensures thorough oxidative decomposition of residual surfactant without promoting sintering or phase changes in the metal hydroxides.

Afterwards, the as-obtained sample is mixed with Vulcan by ball milling for 30 minutes and 350 rpm (1 : 1 in weight) to obtain the metal oxide–carbon composite named La/Mn/Co-200-C. To simplify the nomenclature, the sample before being tested in the ZAB will be referred to as "Fresh" while after its use in the ZAB during the long-term stability charge–discharge test, the sample will be referred to as "Used".

2.3. Characterization techniques

The X-ray diffraction (XRD) analysis was conducted using a Bruker D8-Advance diffractometer (Billerica, USA). The system featured a KRISTALLOFLEX K 760-80F X-ray generator with a voltage range of 20–60 kV and a current range of 5–80 mA, employing Cu Kα radiation as the X-ray source. Data acquisition was performed over a 2θ range of 10° to 80°, with a step size of

0.05°. The crystallite size (D_c) of the materials was estimated using the Scherrer equation (eqn (1)).[34]

$$D_c = \frac{k\lambda}{\beta\cos(\theta)} \quad (1)$$

In this equation, the shape factor constant (k), which accounts for grain morphology, was set to 0.89, while the wavelength of the employed radiation source (λ) was 0.15406 nm. The calculation also incorporated the full width at half maximum (FWHM) of the diffraction peak (β) and the Bragg angle (θ). To compensate for instrumental broadening, the measured FWHM value was corrected by subtracting the instrumental broadening factor, which was determined using a crystalline quartz pattern as a reference. The corrected FWHM value of the sample was then obtained using eqn (2):[34]

$$\beta_{real}^2 = \beta_{obs}^2 - \beta_{inst}^2 \quad (2)$$

where β_{real} is the value obtained from the contribution of the crystallite size, β_{obs} is the measured value, and β_{inst} is the broadening related to the instrument.

X-ray photoelectron spectroscopy (XPS) measurements were carried out using a VG-Microtech Multilab 3000 electron spectrometer (VG Scientific, Sussex, UK), operating within a passing energy range of 2–200 eV. The XPS experiments employed an Al Kα radiation source (1253.6 eV). For binding energy calibration, the C 1s peak at 284.6 eV was used as an internal reference. Data analysis and peak deconvolution were performed using XPSPEAK41 software. Experimental spectra were fitted with Lorentz–Gaussian functions, while the background was modelled using a Shirley-type function.

Density functional theory (DFT) calculations were performed to understand the interaction between Mn and La-based compounds in the electrocatalyst used, as well as to explain the experimental results obtained. The ORCA 5.0. computational package[35] was used to perform the geometry optimizations and energy calculations in conjunction with the def2-TZVP Ahlrichs basis set for light elements and effective core potentials (def2-ECP) for the La heavy element.[36] A geometry pre-optimization was performed using the *meta*-GGA M06L functional,[37] and the geometry obtained was re-optimized using the hybrid B3LYP (hybrid) functional.[38] Solvent effects (water) were simulated using the conductor-like screening model (CPCM) method implemented in ORCA. The $La(OH)_3$ cluster was modelled using the $La_2(OH)_6(OH_2)_{10}$ molecule (La coordination number of 9 [39]), and the Mn_3O_4 species was represented by $Mn_3O_4(OH_2)_8$, employing octahedral and tetrahedral environments by adding water molecules around the Mn atoms to simulate Mn(III) and Mn(II) oxidation states, respectively. The Zn-related species were modelled using the $Zn_2(CH_3CO_2)$ cluster (Zn coordination number = 4 [40]). Regarding the $La(CH_3CO_2)_3$ cluster, it was modelled using the molecule $La_2(CH_3CO_2)_6(OH_2)_{10}$ (La coordination number of 9 [41]). These molecular structures are depicted in Fig. 8.

Scanning electron microscopy (SEM) was utilized to investigate the morphology of the powder samples using a JEOL IT500HR/LA microscope, prior to analysis with the FIB-SEM technique. This instrument is equipped with a field emission gun, providing high-resolution imaging capabilities of 1.5 nm at 30 kV and 4.0 nm at 1 kV. The microscope operates within an accelerating voltage range of 0.5–30 kV.

FIB-SEM tomography was conducted using a Thermo Fisher Scientific Scios 2 DualBeam FIB-SEM system, equipped with an electron beam resolution of 1.4 nm at 1 keV and in an accelerating voltage range of 200 V–30 kV. It was equipped with a Trinity detector system (in-lens and in-column): segmented lower in-lens detector and upper in-lens detector. The ion beam was operated at an accelerating voltage of 30 kV for material removal. Sequential milling was conducted by progressively removing thin material layers from the exposed surface, with each slice having a thickness of 20 nm. Following each milling step, high-resolution SEM imaging was performed to capture the newly exposed surface, generating a series of sequential micrographs with enhanced contrast. Chemical analysis was conducted using an Energy Dispersive X-ray Spectroscopy (EDS) system (Oxford Instruments Ultim Extreme). EDS elemental mapping was performed at regular intervals of every fifth SEM image to provide compositional information throughout the tomographic sequence. Data acquisition was automated using Auto Slice & View 4.2 software. Image stack alignment was performed using the sum of squared differences algorithm without rotation correction in Dragonfly software. Fig. 1 illustrates the setup used for the FIB-SEM technique in which the area in contact with the electrolyte is indicated.

Electrochemical Impedance Spectroscopy (EIS) was conducted between 0.01 Hz and 100 kHz in an Autolab PGSTAT302 potentiostat (Metrohm, The Netherlands) at open circuit voltage (OCV) and at voltages close to the ORR and OER onset, with an amplitude of 10 mV in a ZAB device (2 electrode system). The charge transfer resistance (R_{ct}) was extracted from electrochemical impedance spectroscopy (EIS) data analyzed using Nyquist plots and the Randles equivalent circuit model.[42] The ohmic resistance (R_o) was determined from the Z' intercept at high frequency (100 kHz), and R_{ct} was calculated as the semicircle diameter using $R_{ct} = Z'$ (low frequency) − Z' (high frequency). The ZAB was tested using positive air electrodes composed of the La/Mn/Co-200-C electrocatalyst developed in this study and a commercial catalyst mixture of 20 wt% Pt/C and RuO_2 (1 : 1 weight ratio). These catalysts were prepared as inks containing 0.02 vol% Nafion® and 20 vol% isopropanol in water, which were uniformly applied to the gas diffusion layer carbon paper (QUINTECH, Freudenberg H23C6) using a brush to achieve a mass loading of 1.3 mg cm^{-2}. The negative electrode consisted of polished Zn foil (ThermoScientific, 99.98%). The electrolyte was an aqueous solution of 6 M KOH and 0.2 M $Zn(CH_3CO_2)_2 \cdot 2H_2O$. Both electrodes had a geometrical area of 2.6 cm^2. Battery performance was evaluated using an ARBIN multi-channel SCTS battery testing potentiostat. Polarization curves were recorded at a scan rate of 1 mA s^{-1}, while galvanostatic charge and discharge measurements were performed at 1 mA cm^{-2} with 20-minute charge–discharge cycles. The oxygen introduced into the battery was supplied from the air present in the atmosphere under static conditions, without using any air introduction system.

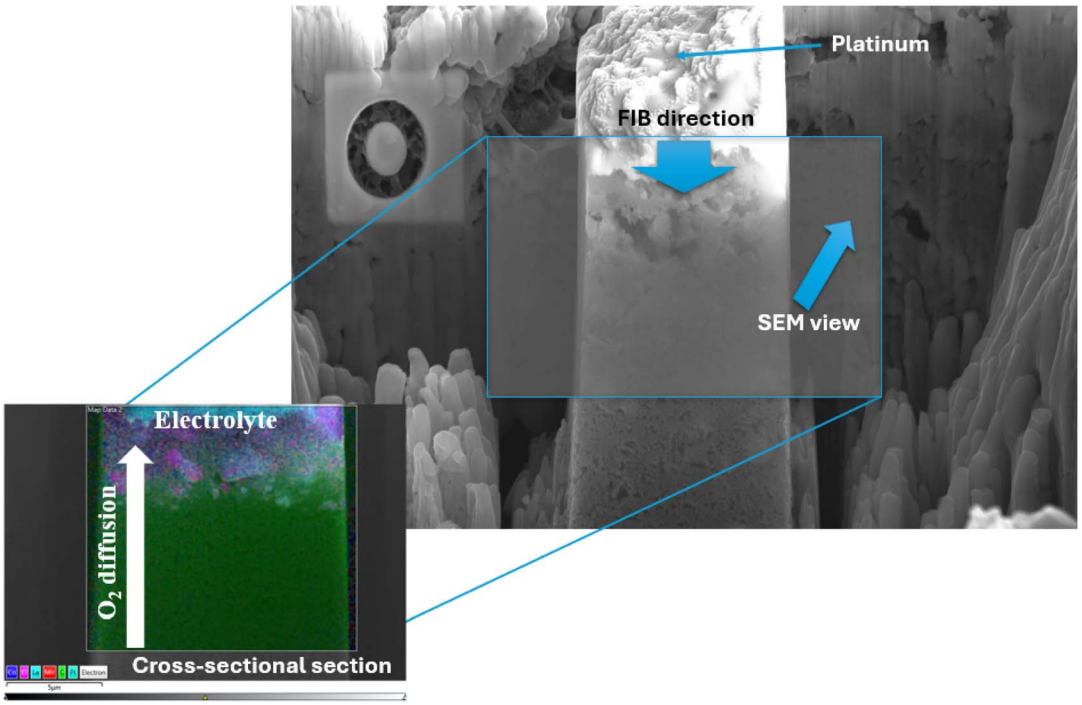

Fig. 1 Set-up used in the FIB-SEM technique. The area in contact with the electrolyte is located at the top, while the area in contact with the oxygen is at the bottom.

3. Results and discussion

This section will discuss the characteristics of the La/Mn/Co-200-C sample before being evaluated in the ZAB, and its electrochemical performance in the ZAB.

3.1. Sample characterization and ZAB performance

The La/Mn/Co-200-C sample demonstrates noteworthy bifunctional activity toward both the ORR and OER, along with remarkable electrochemical parameters in the ZAB using a low-temperature synthesis process at 200 °C. Based on the X-ray diffraction (XRD) results, the sample consists of crystalline phases of $La(OH)_3$ and a minor proportion of hausmannite (Mn_3O_4). The absence of additional Mn or Co-related peaks may be attributed to the high crystallinity of $La(OH)_3$, which overlaps with contributions from low-crystallinity species. The performance in the ZAB can be observed in Fig. 2, showing, in the polarization test, a maximum power of 51 mW cm^{-2} at a current density of 97 mA cm^{-2} (Fig. 2A). Furthermore, the La/Mn/Co-200-C sample exhibits excellent stability and rate performance at different current densities (2, 5, 20, 50 and again 2 mA cm^{-2}) (Fig. 2B) and delivers discharge capacities of 724 and 699 mAh g_{Zn}^{-1} at current densities of 5 and 10 mA cm^{-2}, respectively (Fig. 2C). Based on the results of our previous work,[33] the enhanced performance exhibited by the La/Mn/Co-200-C sample surpasses that of a similar sample without the presence of La, despite $La(OH)_3$ having a high overpotential for ORR/OER. This improvement is attributed to the positive influence of the La^{3+} cation, which induces changes in surface morphology and in the oxidation states of the electroactive species (Mn and Co). Although La^{3+} possesses an empty 4f shell ($4f^0$), its beneficial effect arises from multiple complementary mechanisms:[43] (i) hybridization interactions involving its empty 4f orbitals with the d orbitals of Mn and Co, facilitating intermetal charge transfer; (ii) its role as a soft Lewis acid center, stabilizing the metal oxides; and (iii) the promotion of higher oxidation states of Mn species (particularly Mn(IV)), as evidenced by XPS analysis (Fig. 6A) and confirmed by DFT calculations (Table S1), which demonstrate an increase in partial charges of ~0.2 units for the Mn atoms closest to La. These combined effects enhance electronic conductivity and bifunctional ORR/OER activity.

Fig. 2D illustrates the long-term stability test evaluated at 1 mA cm^{-2} with 20-minute cycles, demonstrating a progressive increase in voltage gap and a short circuit occurring after surpassing 120 h of cycling and more than 360 charge–discharge cycles. To improve the stability of such materials, it is crucial to understand the key factors influencing long-term degradation during cycling.

3.2. FIB-SEM results

The FIB-SEM technique was employed to investigate the changes occurring in the electrocatalyst consisting of La, Mn, and Co metal (hydro-)oxides, along with carbon material, deposited on the GDL *via* drop-casting. Fig. 3 shows the sample before battery use (Fresh) in the upper section, with secondary electron (SE) and backscattered electron (BSE) images at different slices. Similarly, the sample after more than 120 hours of cycling stability testing (Used) is shown in the lower section.

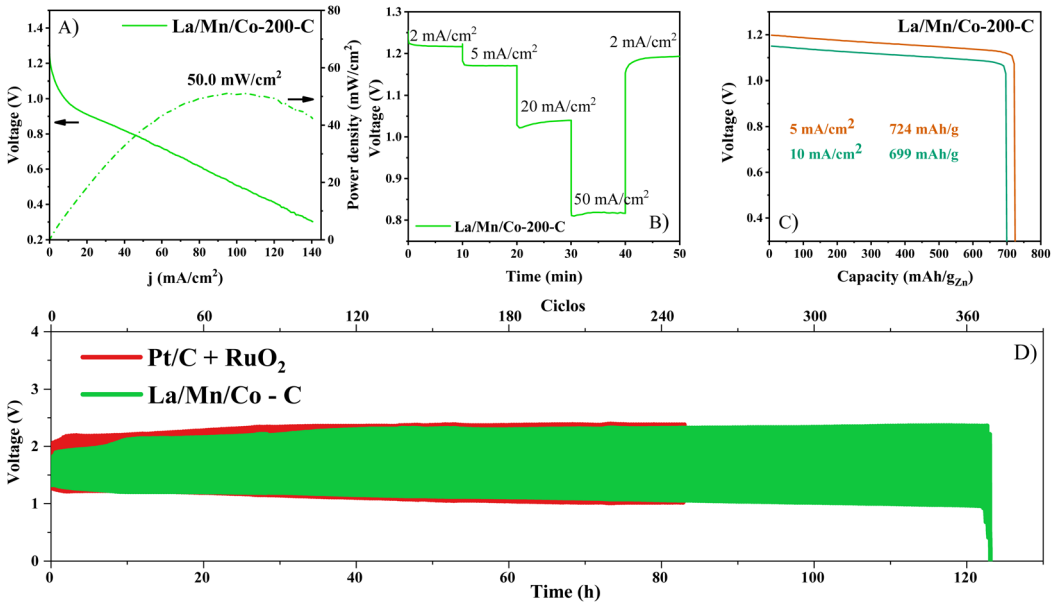

Fig. 2 (A) Polarization and power curves for ZABs prepared with La/Mn/Co-200-C. (B) Reversibility study at current densities of 2, 5, 20, 50 and again 2 mA cm^{-2}. (C) Discharge capacity at 5 and 10 mA cm^{-2}. (D) Long-term stability test at 1 mA cm^{-2} and 20 min charge–discharge cycle.

In the Fresh sample, SE images reveal that the deposited electrocatalyst layer on the GDL is compact and has a thickness of approximately 5 μm. Some small voids are detected between larger particles generated in the electrode preparation process. This trend remains consistent as the number of slices increases (Fig. 3 and Video S1). BSE images reveal elemental composition, where heavier elements appear brighter due to their higher atomic number. Thus, the bright areas correspond to La, Mn, and Co elements. In the Fresh sample, a homogeneous distribution of elements is detected in the outer region of the GDL and a heterogeneous distribution in the inner region, forming irregular agglomerates of metal oxide nanoparticles approximately 1–2 μm in length. The larger nanoparticles detected by BSE coincide with the shape of the nanoparticles detected by SE,

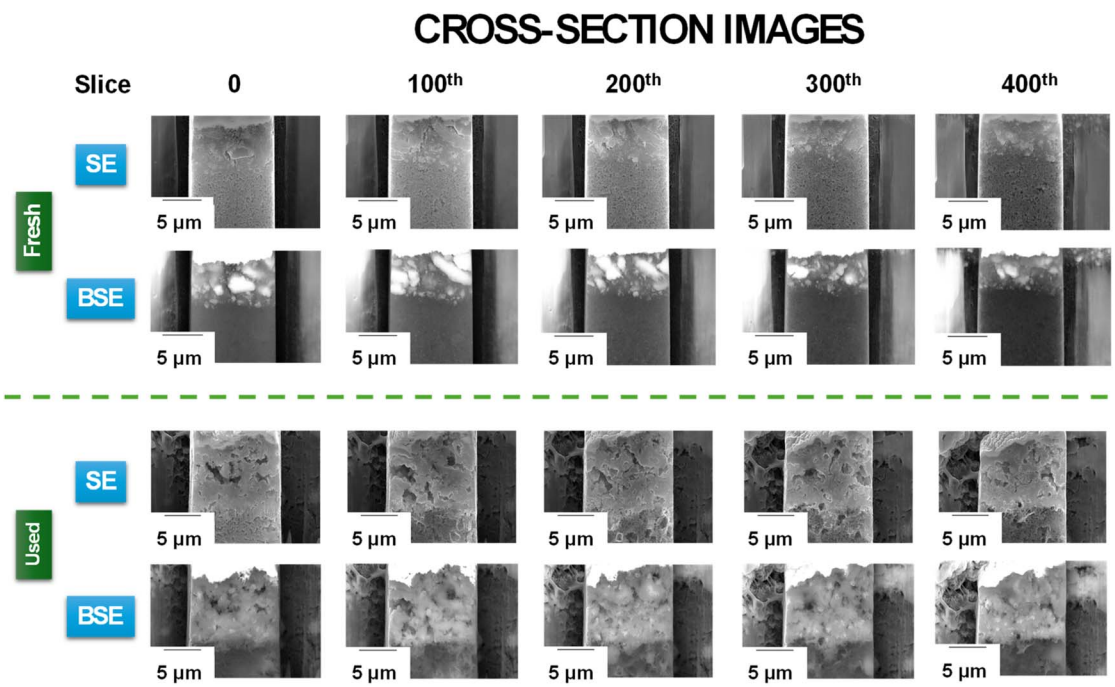

Fig. 3 Cross section images from the Fresh and Used samples with secondary electrons (SEs) and backscattering electrons (BSEs) at different FIB slices. The term "slices" refers to the number of cuts made by the FIB.

between which small pores were detected. This indicates that the nanoparticles of the metal (hydro-) oxides tend to agglomerate at the nanometer scale during the electrocatalyst layer preparation process on the GDL.

When analyzing the Used sample (lower section of Fig. 3 and Video S2), significant differences are observed. First, SE images no longer show a compact layer, and pores and voids of irregular shapes and sizes are observed that can be a consequence of the oxidation and corrosion of the GDL. Quantitatively, the electrode thickness increases from ~5 μm (Fresh) to ~10 μm (Used), with a concurrent dramatic increase in porosity from an estimated ~10–15% (Fresh, characterized by small interstitial voids between particles) to ~40–50% (Used, characterized by extensive irregular pores and void networks). This represents a change in porosity of ~25–35 percentage points, which corresponds to a relative increase of 2–4 fold over the baseline. Such an increase in porosity is expected to decrease ionic conductivity in the electrolyte-filled pores, consistent with the substantial impedance increase observed in EIS (Fig. 7). Additionally, oxygen diffusivity through the GDL is expected to decrease due to the irregular pore structure and increased tortuosity, significantly limiting the kinetics of the ORR. The combination of reduced ionic conductivity, severely hindered oxygen diffusion, and the formation of lanthanum acetate species together account for the dramatic performance degradation and eventual cell failure after 120 hours of cycling.

Regarding the distribution of the metal (hydro)-oxides, it can be observed that the metals distribute in a wider region compared to the fresh materials. Thus, the thickness of the layer of metal oxides on the GDL increases to nearly 10 μm, and it is difficult to provide a precise value due to the lack of a well-defined electrocatalyst-GDL interface.

BSE images reveal an increase in the thickness of the outer region and a more uniform distribution of the elements in the inner region, with less pronounced elemental segregation compared to the Fresh sample, and the electrocatalyst layer extends to larger distances than for the Fresh sample. Additionally, not only irregularly shaped circular nanoparticles are detected, but also thin rods with lengths less than 1 μm are observed in the region of the GDL far from the electrolyte. Thus, charge–discharge cycling produces a redistribution of the metal (hydro)-oxides, giving rise to a lower concentration electrocatalyst distribution in the inner regions of the GDL, and reduces the size of the metal oxide nanoparticles not only on the GDL surface but throughout the entire thickness of the GDL.

At this point, it is crucial to obtain more specific information on the elemental distribution. Therefore, elemental mapping of Mn, Co, La, and Zn was performed (Fig. 4). The EDS elemental mapping images show a homogeneous distribution of Mn and Co in both the Fresh and Used samples, although for both elements an increased depth penetration into the GDL is observed in the Used sample, with elements permeating the GDL to around 2 μm. La exhibits a different behavior, with greater permeability into the GDL, up to ~15 μm (nearly the entire length of the GDL). Notably, a region of higher La concentration at approximately 7 μm from the GDL surface is observed, which is parallel to the GDL surface that is in contact

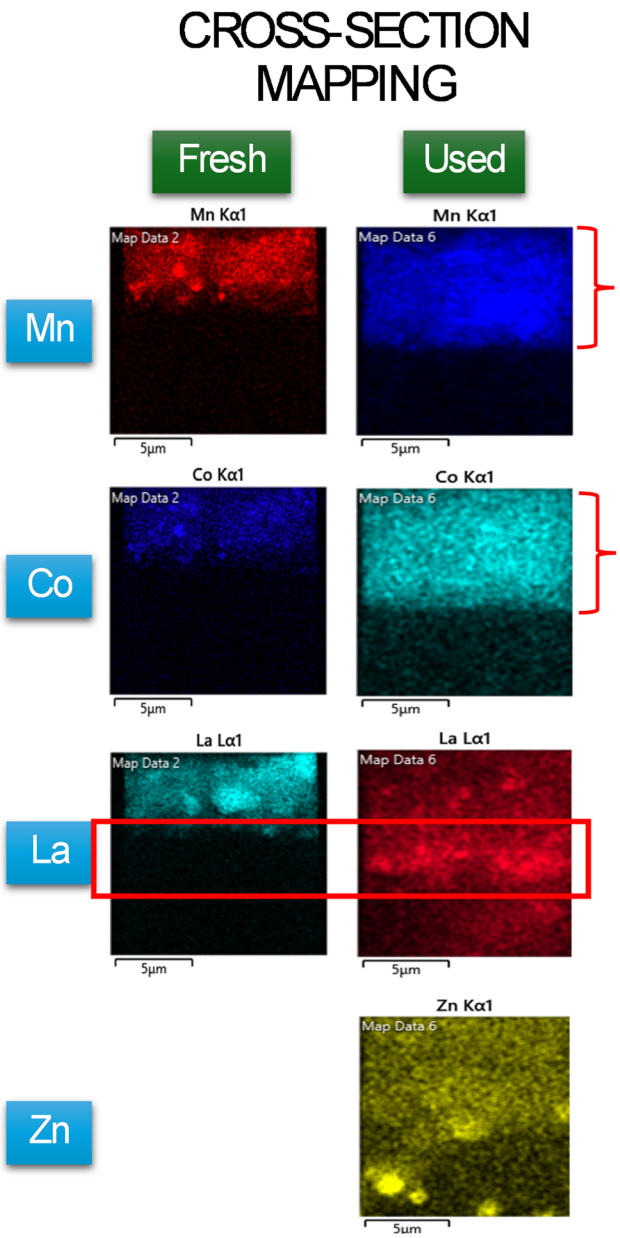

Fig. 4 Cross sectional mapping of the Fresh and Used samples for the Mn, Co, La and Zn elements.

with the electrolyte. This specific location is significant from a transport and electrochemical perspective: at 7 μm (representing ~70% of the total electrode depth in the Used sample), the accumulated lanthanum acetate species forms a percolating barrier that effectively blocks ionic and electronic transport pathways connecting the catalytically active zone near the electrolyte interface (0–2 μm, where Mn and Co remain concentrated) with deeper electrode regions. This positioning creates a bottleneck for charge transfer, explaining the dramatic increase in impedance observed in the EIS measurements (discussed later). If La redistribution were to occur at shallower depths (*e.g.*, 5 μm), less impact on overall conductivity would be expected due to the availability of alternative conduction

pathways. Conversely, if redistribution occurred deeper (*e.g.*, 10 μm near the GDL interface), the impact would be primarily limited to GDL-internal transport, with the active catalytic layer remaining relatively less affected.

The observed redistribution for La can be a consequence of dissolution–precipitation processes, although this phenomenon will be discussed later in more detail. Regarding Zn, its presence is detected across nearly the entire GDL in the Used sample, indicating that the electrolyte permeates the entire structure. However, this permeation does not occur uniformly, as preferential circular regions of approximately 1 μm in diameter are detected in the outermost areas (far from the electrolyte) of the GDL.

The internal structure of the electrodes is most effectively visualized through 3D reconstruction rendered electronically with computer software or presented as a video. For illustration purposes, snapshots from the video are provided in Fig. 5. Thus, in Fig. 5A and B, the 3D reconstructions of the Fresh and Used samples, respectively, are shown. The upper part of the reconstruction corresponds to the area in contact with the electrolyte, while the lower part represents the region through which O_2 diffuses. From the reconstruction analysis of the Fresh sample (Fig. 5A and Video S3), it is evident that the electrocatalyst, characterized by an irregular nanoparticle morphology, is uniformly deposited on the GDL. Subsequently, for the Used sample (Fig. 5B and Video S4), an increased permeability of the electrocatalyst within the GDL is clearly observed, along with the formation of pores and voids in the GDL. These structural changes may modify and even hinder O_2 diffusion making it more inefficient.

To gain a clearer understanding of the elemental distribution, 3D reconstruction of the EDS mapping images was also performed (see Fig. 5C, D and SI Videos). Specifically, Fig. 5C and D highlight snapshots of the La element mapping for the Fresh and Used samples, respectively. These images reveal differences in La permeability, while the distribution of other elements remains less modified, as previously discussed and illustrated in Fig. 4. It should be noted that during the reconstruction, the La concentration was considered homogeneous in all regions where it was present. However, as previously

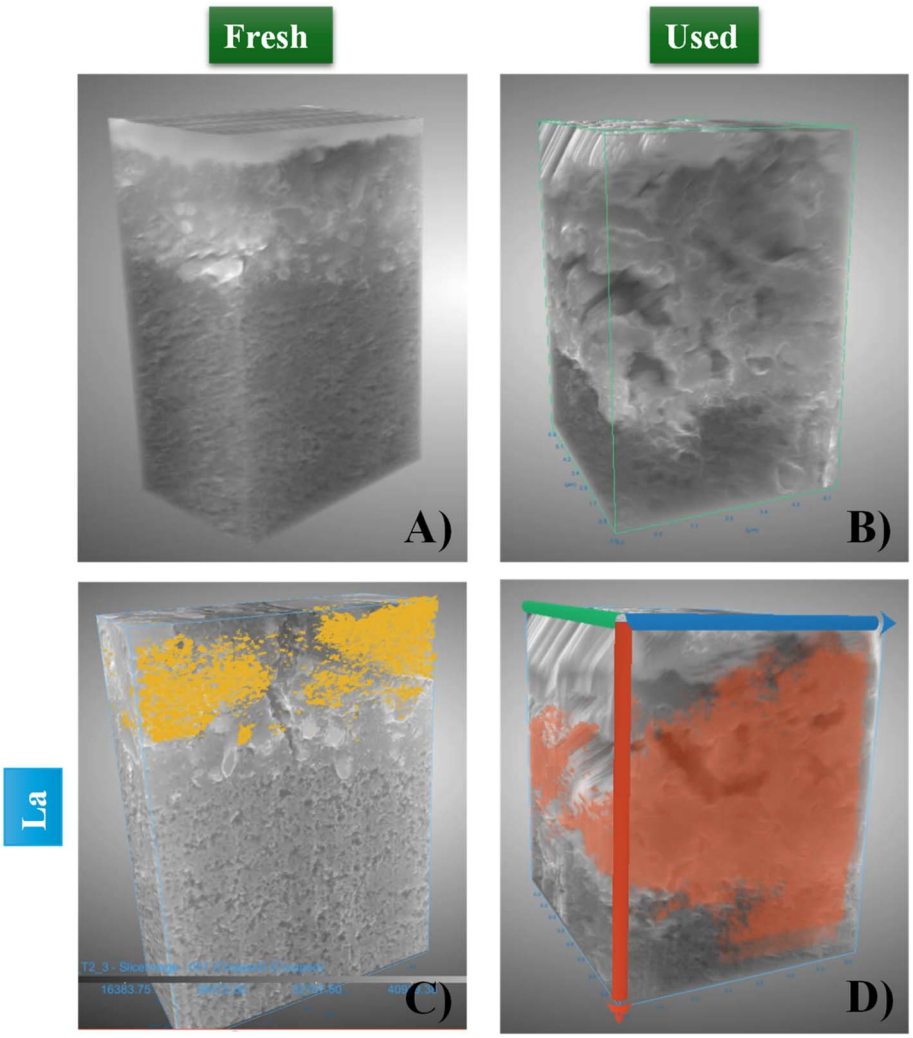

Fig. 5 3D reconstruction of the electrodes for samples: (A) Fresh and (B) Used. And La elemental mapping distribution for (C) Fresh and (D) Used samples.

discussed, Fig. 4 indicates the existence of a region parallel to the GDL surface that is in contact with the electrolyte, with higher La concentration.

3.3. XPS characterization

The XPS analyses of the Fresh and Used samples were conducted. Fig. 6 shows the deconvolution of the Mn 2p, Co 2p, C 1s, and O 1s spectra. The deconvoluted Mn 2p spectrum (Fig. 6A) exhibits two asymmetric peaks associated with Mn $2p_{3/2}$ and Mn $2p_{1/2}$. The Mn $2p_{3/2}$ signal is further resolved into three contributions at approximately 641.3 eV (Mn(II)), 642.6 eV (Mn(III)), and 644.6 eV (Mn(IV)).[44,45] The Mn $2p_{1/2}$ signal is divided into 652.7 eV (Mn(II)), 654.0 eV (Mn(III)), and 656.1 eV (Mn(IV)). In the Fresh sample, the results show a mixture of the three species, with Mn(III) being predominant; and no significative changes are detected in the Used sample. Regarding the Co 2p spectrum (Fig. 6B), a pair of asymmetric peaks associated with Co $2p_{3/2}$ and Co $2p_{1/2}$ is observed, respectively. The Co $2p_{3/2}$ and Co $2p_{1/2}$ signals are divided into two peaks assigned to Co(III) (at 780.7 and 795.9 eV) and Co(II) (at 782.3 and 797.2 eV).[46,47] Similar to the Mn 2p spectrum analysis, the results show no significant differences between the Fresh and Used samples, obtaining a mixture of Co(III) and Co(II) oxidation states, with Co(III) species being predominant. In the case of O 1s (Fig. 6C), five contributions are detected in the deconvoluted spectrum of the Fresh sample. The peak at 531.4 eV corresponds to adsorbed oxygen species in the metallic (hydro-)oxides (O_{ADS}). The peaks at 532.2 and 533.5 eV are associated with C–O and C=O species from the carbon material, respectively, while the peak at 532.8 eV is related to M–O–C species between the metal (hydro-) oxides and the carbon material.[48,49] Finally, the peak located at 535.5 eV is associated with the O–F species[50] from Nafion, which is used as a binder in the electrode preparation. The results for the Fresh sample identify the presence of O_{ADS} species in the metallic (hydro-)oxides, with a greater contribution of C–O species compared to C=O. However, when analyzing the deconvoluted O 1s spectrum of the Used sample, a new peak is detected at 530.0 eV, associated with lattice oxygen (O^{2-}) (O_{LAT}). These new oxygen species are formed from adsorbed oxygen species as a consequence of changes in the electrocatalyst caused by the redistribution of La, and the dioxygen reactions, which facilitate the formation of metal oxide species. A possible reaction scheme for the transformation of O_2 is shown in eqn (3)–(6).[51] The O_{LAT}/O_{ADS} ratio in the Used sample is 0.57 (Table 1), highlighting the significance of the change in the nature of

Table 1 Oxygen-related species ratios obtained from the XPS data

Sample	O_{LAT}/O_{ADS}	O_{C-O}/O_{ADS}	O_{M-O-C}/O_{ADS}	$O_{C=O}/O_{C-O}$
Fresh	—	0.81	0.18	0.37
Used	0.57	0.46	0.07	0.86

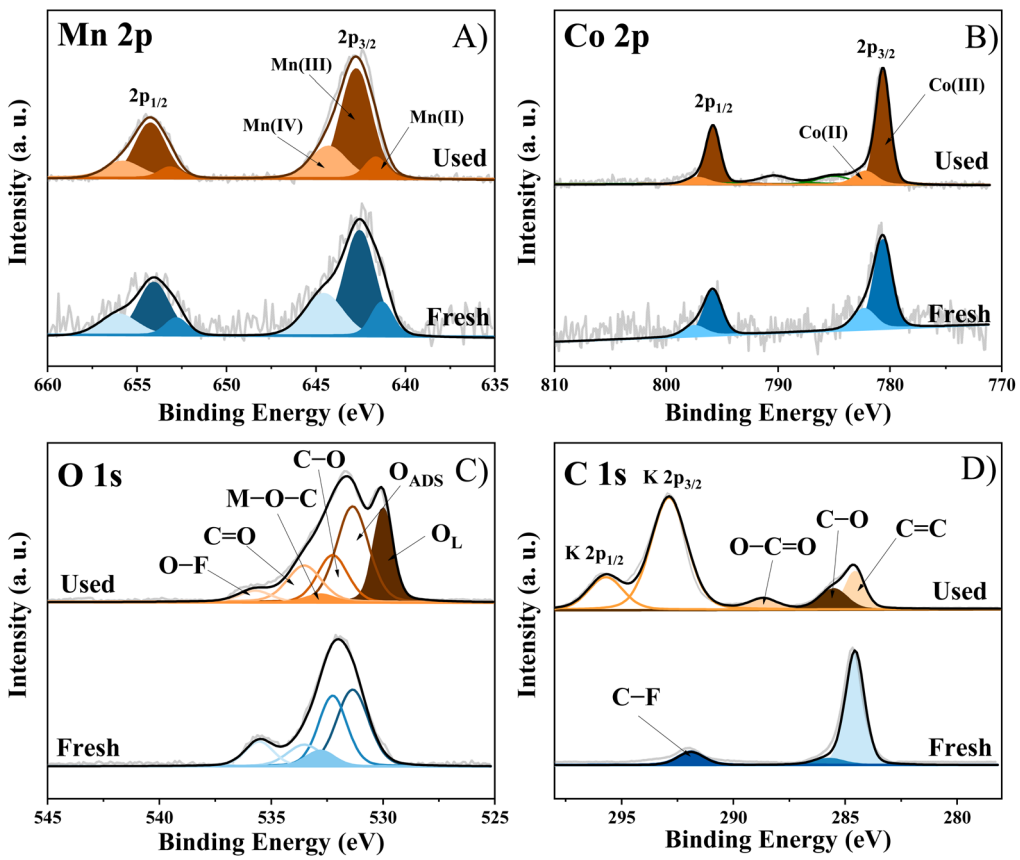

Fig. 6 XPS high-resolution deconvoluted spectra of (A) Mn 2p, (B) Co 2p, (C) O 1s and (D) C 1s of the Fresh and Used samples.

oxygen species within the metallic (hydro-)oxides. This ratio indicates progressive transformation of adsorbed oxygen into lattice oxygen during cycling, driven by La redistribution and successive ORR events. While increased O^{2-} species can theoretically facilitate lattice oxygen-mediated OER *via* direct O–O coupling and enhanced ORR through modified electronic structure and reduced oxygen vacancy formation energy,[52] this potential benefit is offset by the simultaneous formation of inactive lanthanum acetate species, increased impedance (Fig. 7), and GDL permeation. The net effect is a trade-off between potential lattice oxygen mechanistic contributions and substantial loss of active La–Mn synergistic sites, explaining the observed ORR activity degradation despite O_{LAT} formation.

In the Used sample, an increase in C=O species is detected compared to the Fresh sample: the $O_{C=O}/O_{C-O}$ ratio increases from 0.37 to 0.86. The increase in oxidized species reflects the influence of oxidative processes (ZAB charging process) on the carbon material.

Finally, a decrease in the contribution of M–O–C species is observed (Table 1), indicating a decrease in the interaction between the metallic (hydro-)oxides and the carbon material, likely caused by the chemical changes in both materials.

$$O_2 + e^- \rightarrow O_2^- \quad (3)$$

$$O_2^- + e^- \rightarrow O_2^{2-} \quad (4)$$

$$O_2^{2-} \rightarrow 2O^- \quad (5)$$

$$2O^- + 2e^- \rightarrow 2O^{2-} \quad (6)$$

Fig. 6D shows the deconvoluted C 1s spectra. The deconvoluted spectrum reveals that in the Fresh sample, two contributions are identified at 284.6 and 285.7 eV, corresponding to C=C and C–O bonds,[53] respectively, as well as a contribution at 291.9 eV associated with the C–F species from the Nafion binder.[50] In the Used sample, an additional peak at 288.7 eV is observed, corresponding to the O–C=O species.[54] The presence of K $2p_{3/2}$ and K $2p_{1/2}$ peaks at 292.9 and 295.7 eV,[55] originating from the KOH-based electrolyte, appears at binding energies sufficiently separated from the carbon-related peaks to allow accurate deconvolution without interfering with the quantification of oxidized carbon species. The separation of ~4–8 eV between the C–O/O–C=O peaks (284.6–288.7 eV) and the K 2p peaks (292.9–295.7 eV) ensures reliable peak fitting using Lorentz–Gaussian functions with Shirley-type background correction. This is further supported by the concurrent detection of O–C=O species in the O 1s spectrum (Fig. 6C) at 288.7 eV, which independently corroborates the oxidation of the carbon material. Moreover, the peak associated to C–O species increases importantly because of an extensive oxidation of the carbon material. Additionally, the peak associated with O–C=O can be attributed to acetate (eqn (7))[56] and/or carbonate species (eqn (8)). Thus, the observed redistribution of La detected in Fig. 4 can be a consequence of dissolution–precipitation processes generated by the interaction with the electrolyte and promoted by the local changes in pH that may occur during the charge and discharge processes or by complexation with acetate species coming from the electrolyte; CH_3COO^- and OH^- ions are ligands that can interact with lanthanum in alkaline medium increasing its solubility.[56,57] This process results in the formation of the region observed with higher concentration of La, which may affect the electrochemical behavior because of changes in the conductivity of the electrode and in the intrinsic electrocatalytic activity of the metal (hydro)-oxides. According to our previous work,[33] Mn and Co are the most electroactive elements for the ORR and OER, in which lanthanum seems to play a stabilizing role that might be crucial for the performance of the electrocatalysts.

$$La^{3+} + nCH_3COO^- \leftrightarrow La(CH_3COO^-)_n^{(3-n)+} \quad (7)$$

$$C + 6OH^- \rightarrow CO_3^{2-} + 3H_2O + 4e^- \quad (8)$$

However, the formation of carbonate species either because of the corrosion of the carbon material or from the carbonation of the electrolyte cannot be ruled out, and this process will also contribute to the degradation of the performance of the ZABs. It has been reported that carbonate formation in ZABs accelerates the decrease of the discharge voltage to the cutoff value, leading to a shortened cycle life of the rechargeable ZAB. Furthermore,

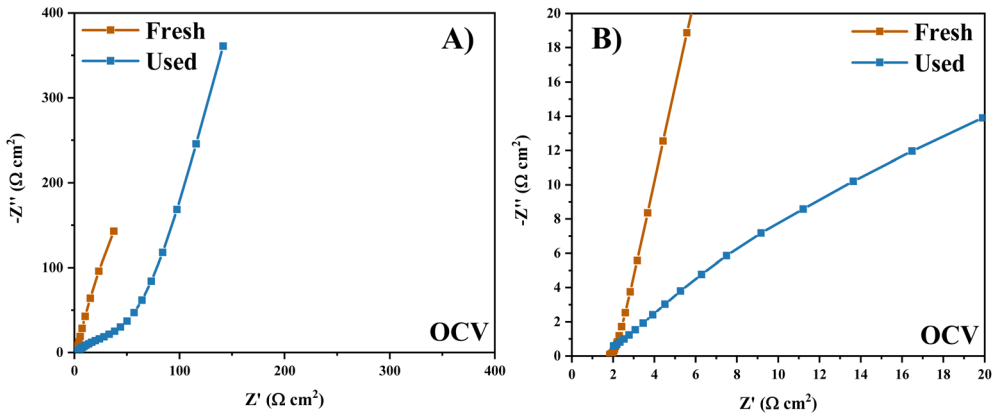

Fig. 7 (A) EIS plot at OCV for the Fresh and Used sample. (B) High-frequency region of the EIS plot.

carbonate formation impedes the OER during charging due to a reduced concentration of OH^-, and promotes ZnO formation, also driven by the local depletion of OH^-.[58,59] However, the formation of lanthanum carbonate is not likely to significantly decrease the electrocatalytic activity toward the ORR, as studies have reported the formation of covalent bonds between $La_2O_2CO_3$ and carbon material at the interface, which can act as active sites for the ORR.[48,60]

The XPS spectrum of La 3d (Fig. S1) for the Fresh sample shows two regions at ~835 and ~851 eV, corresponding to La $3d_{5/2}$ and La $3d_{3/2}$, respectively. The deconvolution of this spectrum is difficult due to contributions related to changes in the 4f orbitals of La[43] making the analysis and assignment to specific compounds challenging. In these regions, two peaks are detected with a separation of approximately 3.9 eV, which is associated with the presence of $La(OH)_3$, as confirmed by XRD analysis. However, the spectrum for the Used sample changes significantly. Specifically, the region at around ~839.5 eV, associated with electron transfer from the ligand to La bonding orbitals[33,61] is quite different in the Used sample compared to the Fresh sample, indicating modifications in the La coordination sphere. Therefore, the chemical environment of La is strongly modified in the Used sample, in agreement with the important changes in its distribution within the GDL because of the interaction with the electrolyte.

To evaluate differences in the conductivity of the Fresh and Used samples due to the formation of lanthanum acetate/carbonate species, EIS experiments were performed at open circuit voltage and at voltages near the onset potentials of the ORR and OER. Fig. 7A displays the EIS results at OCV, and Fig. 7B presents the high-frequency region, revealing significant differences between the samples. A substantial increase in resistance is observed in the Used sample, which may be caused by the redistribution of La species, that are less interacting with Mn and Co compounds, leading to the formation of the observed lanthanum carbonate/acetate layer that increases electrode resistance, and also to the GDL deterioration. This trend is consistently observed in the EIS measurements at the different potentials tested for the ORR–OER processes (Fig. S2). Quantitative analysis of the EIS data at OCV reveals a selective increase in charge transfer resistance (R_{ct}). The Nyquist plots demonstrate that the charge transfer resistance increases from 1.7 Ω cm^2 (Fresh) to 136 Ω cm^2 (Used), representing a 79-fold increase. In contrast, the ohmic resistance increases only moderately from 9.3 Ω cm^2 to 12.6 Ω cm^2, respectively, indicating that the degradation mechanism is localized at the electrode–electrolyte interface rather than affecting bulk conductivity. The Warburg impedance (representing oxygen diffusion impedance) also increases 10-fold, from 7.5 Ω cm^2 (Fresh) to 75 Ω cm^2 (Used), indicating that the lanthanum acetate barrier simultaneously impedes both charge transfer and oxygen diffusion. This selective increase in R_{ct} directly translates to an increase in overpotential. Therefore, we attribute a significant contribution to the decrease in electrocatalytic activity to the formation of inactive lanthanum acetate species, which can reduce the conductivity in the GDL, modify the properties of Mn and Co compounds and may also prevent efficient diffusion of O_2 because of its redistribution in the GDL.

3.4. DFT calculations

To corroborate experimental observations, DFT calculations were performed, including structural optimization and energy profiling. Initially, the interactions between $La(OH)_3$ and Mn_3O_4 compounds were investigated. Subsequently, since there is evidence for the formation of $La(CH_3COO)_3$ species in the sample after electrochemical cycling, originating from $Zn(CH_3COO)_2$ species present in the electrolyte, the energy change associated with acetate species formation from the initial Mn–La-containing cluster was also examined.

The Mn_3O_4 species contains Mn atoms in +2 and +3 oxidation states, arranged in tetrahedral and octahedral coordination environments, respectively. Therefore, DFT calculations were first performed to evaluate the energy of the interaction between $La(OH)_3$ and Mn_3O_4, considering bonding through either a Mn(II) atom (tetrahedral coordination) or a Mn(III) atom (octahedral coordination). For this purpose, the starting Mn and La-containing clusters were simulated by incorporating H_2O molecules and optimizing the resulting structures, optimized to $Mn_3O_4(OH_2)_8$ and $La_2(OH)_6(OH2)_{10}$ clusters for Mn_3O_4 and $La(OH)_3$, respectively. Although La^{3+} formally possesses an empty 4f shell ($4f^0$ configuration), its vacant 4f orbitals can participate in electronic hybridization with the d orbitals of neighboring transition metals, facilitating favorable charge redistribution as evidenced by the calculated partial charges (Table S1).

The results obtained from the clusters formed by the interaction through the tetrahedral and octahedral Mn coordination, demonstrate that both configurations exhibit negative stabilization energies (Fig. 8). However, a stronger interaction is observed when $Mn_3O_4(OH_2)_8$ binds to $La_2(OH)_6(OH_2)_{10}$ *via* a Mn(II) atom (−4.8 eV), compared to bonding through a Mn(III) atom (−2.9 eV) (Fig. S3).

The stability of the La–Mn interaction *via* Mn(II) sites (−4.8 eV) *versus* Mn(III) sites (−2.9 eV) establishes a thermodynamic preference for bonding pathways. The 1.9 eV difference represents a significant energetic favorability toward Mn(II) coordination. To assess the sensitivity of this preference, a hypothetical scenario where the Mn(II) interaction energy decreases to −4.0 eV would reduce the energy difference between Mn(II) and Mn(III) pathways from 1.9 eV to 1.1 eV. While Mn(II) coordination would still be thermodynamically favored, the reduced energy gap would shift the equilibrium distribution toward increased population of Mn(III)-mediated clusters. This shift has important implications: Mn(III)-coordinated clusters exhibit lower partial charge redistribution and retain lower oxidation states compared to Mn(II)-bridged clusters. The consequence would be a mixed population of La–Mn clusters with variable electronic properties and reduced average conductivity. In the actual system with $\Delta E = -4.8$ eV, the large energy difference strongly favors Mn(II) coordination, ensuring homogeneous cluster populations with optimized electronic properties. This thermodynamic hierarchy explains why the La–

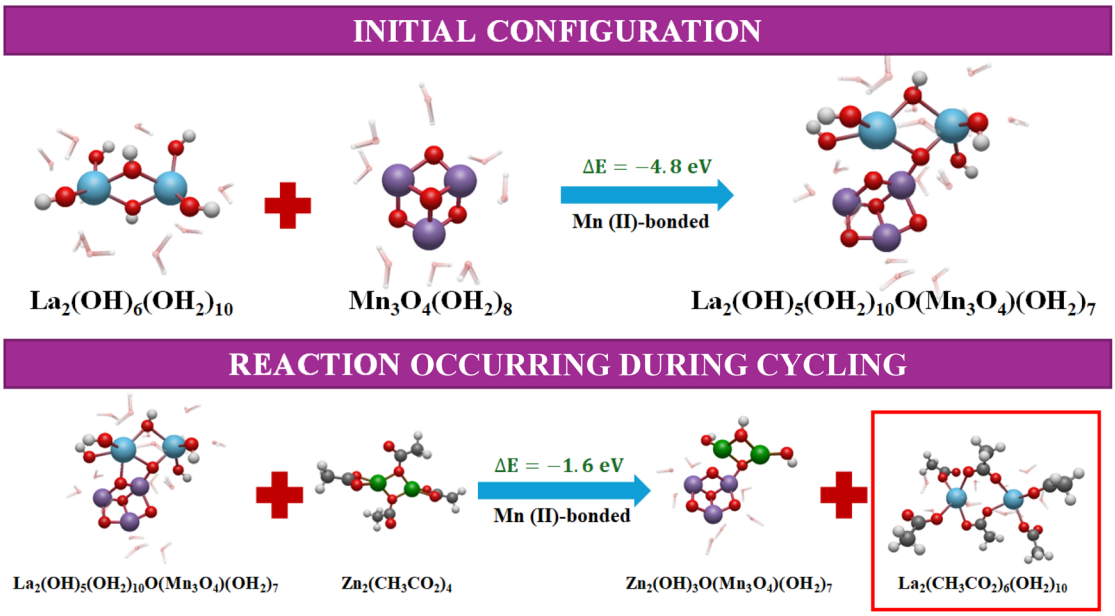

Fig. 8 Schematic representation of the results obtained from structural optimization and stabilization energy for the initial configuration and the reaction occurring during cycling in the ZAB. The opacity of the coordinated water molecules has been reduced to enhance the visualization of the molecule but without modifying the coordination number. The color code is as follows: La (blue), Mn (purple), O (red), H (white) and Zn (green).

Mn electrocatalyst in the Fresh sample exhibits bifunctional ORR/OER activity: the strong preference for Mn(II) interaction promotes uniformly high oxidation states (Mn(IV)) that enhance electronic conductivity. A hypothetical weakening of the Mn(II) interaction to −4.0 eV would result in a heterogeneous distribution of La–Mn cluster types, degrading the average electrocatalytic performance and increasing the vulnerability of the system to further degradation pathways.

Table S1 presents the partial charges of La and Mn atoms in the resulting La–Mn clusters, as well as in the initial clusters. The results show an increase in partial charge of approximately 0.2 units for both La and Mn upon cluster formation, with a more pronounced increase observed for the Mn atom closest to the La cluster. This increase in partial charge may influence the initial steps of the ORR and OER mechanisms and is associated with a higher oxidation state of Mn species, particularly related to Mn(IV) species, which have been shown to enhance electronic conductivity and, consequently, the bifunctional ORR/OER electrocatalytic activity.[62]

As revealed by FIB-SEM analysis, in the used samples, lanthanum is distributed throughout the majority of the GDL, along with zinc, demonstrating that the electrolyte ($Zn(CH_3COO)_2$) permeates the entire GDL. This leads to the formation of lanthanum acetate species, which are responsible for modifying the initial La–Mn interaction that originally exhibits adequate electroactivity. Therefore, we have calculated the change in energy for the reaction between the La–Mn cluster ($La_2(OH)_5(OH_2)_{10}O(Mn_3O_4)(OH_2)_7$) and zinc acetate from the electrolyte, resulting in the formation of lanthanum acetate and a Zn–Mn cluster.

The molecule chosen to simulate the electrolyte is $Zn_2(CH_3COO)_4$, possessing a structure analogous to the previously studied La–Mn clusters. The results indicate that, for an initial interaction *via* Mn(II) atoms with $La_2(OH)_6(OH_2)_{10}$, previously identified as the most favorable scenario, a change in energy of −1.6 eV is obtained for the reaction with the Zn acetate (Fig. 8). This finding demonstrates that the La–Mn cluster may react in the presence of $Zn_2(CH_3COO)_4$ species from the electrolyte, leading to the formation of a Mn–Zn cluster with the formula $Zn_2(OH)_3O(Mn_3O_4)(OH_2)_7$ and La acetate species which have some solubility.[56,57]

Fig. S3 shows that this interaction is also favorable when manganese initially binds to lanthanum through Mn(III) atoms. Regarding the Mulliken partial charges (Table S1), lanthanum acetate displays values similar to those of lanthanum hydroxide. In contrast, the Zn–Mn cluster shows slightly higher partial charges on the Mn atoms, particularly on the Mn atom bridging the Zn cluster, although this effect is less pronounced than in the La–Mn cluster.

Our DFT calculations demonstrate that in the presence of a zinc acetate electrolyte, the energetically favorable formation of lanthanum acetate alters the crucial La–Mn interaction, which is essential for electrocatalytic activity.

4. Conclusions

The FIB-SEM technique has been employed for the first time to study the degradation of the positive electrode in ZAB analyzing the changes occurring in the catalyst-containing GDL samples before and after the galvanostatic cycling stability evaluation stability test in the ZAB. The results revealed different behaviors among the metals constituting the metal (hydro-)oxides in the electrocatalyst material after its use: Mn and Co, the active materials for the ORR/OER, were predominant in the region

near the electrolyte, while La redistributed in a region farther from the electrolyte forming a wider region. This La redistribution can be due to complexation reactions with acetate anions originating from the electrolyte. Additionally, surface morphology differences were observed, with a greater number of pores detected in the Used sample, which is probably a consequence of GDL deterioration.

XPS analysis confirms the presence of acetate species, as well as strong oxidation of the carbon material as a consequence of its deterioration and further corrosion. Through DFT calculations, it has been demonstrated that the formation of lanthanum acetate species is energetically favorable from the initial (hydro-)oxide species of manganese and lanthanum. Therefore, this study highlights that the different behaviours of the metals in the cathode electrocatalyst of ZABs in the presence of the electrolyte allow the understanding of electrochemical degradation, underscoring the importance of the electrocatalyst-GDL interface. Moreover, we can conclude that the FIB-SEM technique is very powerful for following the changes occurring at the micro/nanoscopic level, which is very useful for understanding the fate of electrocatalysts during their use.

Conflicts of interest

The authors declare that they have no known competing financial interests or personal relationships that could have appeared to influence the work reported in this paper.

Data availability

Data for this article, including the figures, images and videos are available at https://doi.org/10.5281/zenodo.17876240.

Supplementary information (SI) is available. See DOI: https://doi.org/10.1039/d5ta10107g.

Acknowledgements

The authors would like to thank the PID2022-137566OB-I00 project funded by MCIN/AEI/10.13039/501100011033 and "ERDF/EU". M. García-Rodríguez thanks Ministerio de Universidades for the FPU20-01746 grant. The LUCENTUM cluster was financed by GV and ERDF/UE (Project IDIFEDER/2021/023). FIB-SEM data were recorded at the facilities of the DME-UCA node of the Spanish Unique Infrastructure for Electron Microscopy of Materials (ICTS, ELECMI) through the project ELC233-2023.

References

1 J. Lee, S. Tai Kim, R. Cao, N. Choi, M. Liu, K. T. Lee and J. Cho, Metal–Air Batteries with High Energy Density: Li–Air versus Zn–Air, *Adv. Energy Mater.*, 2011, **1**, 34–50, DOI: 10.1002/aenm.201000010.

2 V. Caramia and B. Bozzini, Materials science aspects of zinc–air batteries: a review, *Mater. Renew. Sustain. Energy*, 2014, **3**, 28, DOI: 10.1007/s40243-014-0028-3.

3 K. W. Leong, Y. Wang, M. Ni, W. Pan, S. Luo and D. Y. C. Leung, Rechargeable Zn-air batteries: Recent trends and future perspectives, *Renew. Sustain. Energy Rev.*, 2022, **154**, 111771, DOI: 10.1016/j.rser.2021.111771.

4 J.-N. Liu, C.-X. Zhao, J. Wang, D. Ren, B.-Q. Li and Q. Zhang, A brief history of zinc–air batteries: 140 years of epic adventures, *Energy Environ. Sci.*, 2022, **15**, 4542–4553, DOI: 10.1039/D2EE02440C.

5 J. Liu, C. Zhao, D. Ren, J. Wang, R. Zhang, S. Wang, C. Zhao, B. Li and Q. Zhang, Preconstructing Asymmetric Interface in Air Cathodes for High-Performance Rechargeable Zn–Air Batteries, *Adv. Mater.*, 2022, **34**, 2109407, DOI: 10.1002/adma.202109407.

6 N. Shang, K. Wang, M. Wei, Y. Zuo, P. Zhang, H. Wang, Z. Chen and P. Pei, Challenges for large scale applications of rechargeable Zn–air batteries, *J. Mater. Chem. A*, 2022, **10**, 16369–16389, DOI: 10.1039/D2TA04294K.

7 Z. Zhao, X. Fan, J. Ding, W. Hu, C. Zhong and J. Lu, Challenges in Zinc Electrodes for Alkaline Zinc–Air Batteries: Obstacles to Commercialization, *ACS Energy Lett.*, 2019, **4**, 2259–2270, DOI: 10.1021/acsenergylett.9b01541.

8 D. D. Macdonald, The history of the Point Defect Model for the passive state: A brief review of film growth aspects, *Electrochim. Acta*, 2011, **56**, 1761–1772, DOI: 10.1016/j.electacta.2010.11.005.

9 K. Liu, P. He, H. Bai, J. Chen, F. Dong, S. Wang, M. He and S. Yuan, Effects of dodecyltrimethylammonium bromide surfactant on both corrosion and passivation behaviors of zinc electrodes in alkaline solution, *Mater. Chem. Phys.*, 2017, **199**, 73–78, DOI: 10.1016/j.matchemphys.2017.06.050.

10 N. Liu, S. Bi, Y. Zhang, Y. Ou, C. Gong, J. Ran, Y. Chen and Y. Yang, Nanofiber-based polymer electrolyte membranes for fuel cells, *Carbon Energy*, 2025, **7**, e677, DOI: 10.1002/cey2.677.

11 G. McLean, An assessment of alkaline fuel cell technology, *Int. J. Hydrogen Energy*, 2002, **27**, 507–526, DOI: 10.1016/S0360-3199(01)00181-1.

12 S. Hosseini, S. Masoudi Soltani and Y.-Y. Li, Current status and technical challenges of electrolytes in zinc–air batteries: An in-depth review, *Chem. Eng. J.*, 2021, **408**, 127241, DOI: 10.1016/j.cej.2020.127241.

13 M. Mechili, C. Vaitsis, N. Argirusis, P. K. Pandis, G. Sourkouni and C. Argirusis, Research progress in transition metal oxide based bifunctional electrocatalysts for aqueous electrically rechargeable zinc-air batteries, *Renew. Sustain. Energy Rev.*, 2022, **156**, 111970, DOI: 10.1016/j.rser.2021.111970.

14 A. K. Worku, D. W. Ayele and N. G. Habtu, Recent advances and future perspectives in engineering of bifunctional electrocatalysts for rechargeable zinc–air batteries, *Mater. Today Adv.*, 2021, **9**, 100116, DOI: 10.1016/j.mtadv.2020.100116.

15 Q. Han, X. Zhao, Y. Luo, L. Wu, S. Sun, J. Li, Y. Wang, G. Liu and Z. Chen, Synergistic Binary Fe–Co Nanocluster Supported on Defective Tungsten Oxide as Efficient Oxygen Reduction Electrocatalyst in Zinc-Air Battery, *Adv. Sci.*, 2022, **9**, 2104237, DOI: 10.1002/advs.202104237.

16 W. Guo, F. Gu, Q. Chen, K. Fu, Y. Zhong, J. Lv, S. Pan and Y. Chen, Photothermal-boosted flexible rechargeable zinc-air battery based on Ni-doped Mn_3O_4 with excellent low-temperature adaptability, *Carbon Energy*, 2024, **6**, e567, DOI: 10.1002/cey2.567.

17 Z. Liu, C. Yang, R. Jin, S. Li, J. Liu, J. Li, R. Yin, X. Chi, Y. Chen and L. Gao, Fe-Facilitated Deep Reconstruction of Ni_3S_2 Toward Superior Oxygen Evolution, *Carbon Energy*, 2025, e70136, DOI: 10.1002/cey2.70136.

18 Z. Liu, S. Bai, S. Burke, J. N. Burrow, R. Geurts, C.-J. Huang, C. Jiao, H.-B. Lee, Y. S. Meng, L. Novák, B. Winiarski, J. Wang, K. Wu and M. Zhang, FIB-SEM: Emerging Multimodal/Multiscale Characterization Techniques for Advanced Battery Development, *Chem. Rev.*, 2025, **125**, 5228–5281, DOI: 10.1021/acs.chemrev.4c00831.

19 Y.-P. Deng, Y. Jiang, R. Liang, N. Chen, W. Chen, Z.-W. Yin, G. King, D. Su, X. Wang and Z. Chen, Reconstructing 3d-Metal Electrocatalysts through Anionic Evolution in Zinc–Air Batteries, *J. Am. Chem. Soc.*, 2023, **145**, 20248–20260, DOI: 10.1021/jacs.3c03214.

20 C.-C. Weng, X.-W. Lv, J.-T. Ren, Y.-S. Wang, W.-W. Tian, L.-J. Gao, H.-Y. Wang and Z.-Y. Yuan, Self-Promoted Electrocatalysts Derived from Surface Reconstruction for Rechargeable Zinc–Air Batteries, *ACS Sustain. Chem. Eng.*, 2022, **10**, 6456–6465, DOI: 10.1021/acssuschemeng.2c01568.

21 A. Saad, Y. Gao, A. Ramiere, T. Chu, G. Yasin, Y. Wu, S. Ibraheem, M. Wang, H. Guo, P. Tsiakaras and X. Cai, Understanding the Surface Reconstruction on Ternary W_xCoB_x for Water Oxidation and Zinc–Air Battery Applications, *Small*, 2022, **18**, 2201067, DOI: 10.1002/smll.202201067.

22 J. Yu, B. Li, C. Zhao, J. Liu and Q. Zhang, Asymmetric Air Cathode Design for Enhanced Interfacial Electrocatalytic Reactions in High-Performance Zinc–Air Batteries, *Adv. Mater.*, 2020, **32**, 1908488, DOI: 10.1002/adma.201908488.

23 S. Reyntjens and R. Puers, A review of focused ion beam applications in microsystem technology, *J. Micromech. Microeng.*, 2001, **11**, 287–300, DOI: 10.1088/0960-1317/11/4/301.

24 L. Gu, N. Wang, X. Tang and H. G. Changela, Application of FIB-SEM Techniques for the Advanced Characterization of Earth and Planetary Materials, *Scanning*, 2020, **2020**, 1–15, DOI: 10.1155/2020/8406917.

25 Z. Liu, J. Scott Cronin, Y. K. Chen-Wiegart, J. R. Wilson, K. J. Yakal-Kremski, J. Wang, K. T. Faber and S. A. Barnett, Three-dimensional morphological measurements of $LiCoO_2$ and $LiCoO_2/Li(Ni_{1/3}Mn_{1/3}Co_{1/3})O_2$ lithium-ion battery cathodes, *J. Power Sources*, 2013, **227**, 267–274, DOI: 10.1016/j.jpowsour.2012.11.043.

26 J. Z. Lee, T. A. Wynn, M. A. Schroeder, J. Alvarado, X. Wang, K. Xu and Y. S. Meng, Cryogenic Focused Ion Beam Characterization of Lithium Metal Anodes, *ACS Energy Lett.*, 2019, **4**, 489–493, DOI: 10.1021/acsenergylett.8b02381.

27 Y. Sun, Y. Yuan, L. Lu, X. Han, X. Kong, H. Wang, M. Ouyang, P. Gao, H. Zheng and K. Wang, A comprehensive research on internal short circuits caused by copper particle contaminants on cathode in lithium-ion batteries, *eTransportation*, 2022, **13**, 100183, DOI: 10.1016/j.etran.2022.100183.

28 Z. Deng, X. Lin, Z. Huang, J. Meng, Y. Zhong, G. Ma, Y. Zhou, Y. Shen, H. Ding and Y. Huang, Recent Progress on Advanced Imaging Techniques for Lithium-Ion Batteries, *Adv. Energy Mater.*, 2021, **11**, 2000806, DOI: 10.1002/aenm.202000806.

29 M. Biton, F. Tariq, V. Yufit, B. Wu and N. P. Brandon, Advanced 3D Imaging, Analysis and Characterisation of Zn Dendrite Formation in a Zn-Air Battery, *ECS Meet. Abstr.*, 2015, **MA2015-03**, 444, DOI: 10.1149/MA2015-03/2/444.

30 V. Yufit, F. Tariq, D. S. Eastwood, M. Biton, B. Wu, P. D. Lee and N. P. Brandon, Operando Visualization and Multi-scale Tomography Studies of Dendrite Formation and Dissolution in Zinc Batteries, *Joule*, 2019, **3**, 485–502, DOI: 10.1016/j.joule.2018.11.002.

31 M. Biton, F. Tariq, V. Yufit, Z. Chen and N. Brandon, Integrating multi-length scale high resolution 3D imaging and modelling in the characterisation and identification of mechanical failure sites in electrochemical dendrites, *Acta Mater.*, 2017, **141**, 39–46, DOI: 10.1016/j.actamat.2017.09.008.

32 T. Danner, S. Eswara, V. P. Schulz and A. Latz, Characterization of gas diffusion electrodes for metal-air batteries, *J. Power Sources*, 2016, **324**, 646–656, DOI: 10.1016/j.jpowsour.2016.05.108.

33 M. García-Rodríguez, D. Cazorla-Amorós and E. Morallón, Enhanced lanthanum-stabilized low crystallinity metal oxide electrocatalysts with superior activity for oxygen reactions, *Electrochim. Acta*, 2024, **479**, 143858, DOI: 10.1016/j.electacta.2024.143858.

34 Y. Waseda, E. Matsubara and K. Shinoda, *X-Ray Diffraction Crystallography*, Springer, Sendai, Japan, 2011, DOI: 10.1007/978-3-642-16635-8.

35 F. Neese, Software update: The ORCA program system—Version 5.0, *Wiley Interdiscip. Rev.: Comput. Mol. Sci.*, 2022, **12**, e1606, DOI: 10.1002/wcms.1606.

36 F. Weigend and R. Ahlrichs, Balanced basis sets of split valence, triple zeta valence and quadruple zeta valence quality for H to Rn: Design and assessment of accuracy, *Phys. Chem. Chem. Phys.*, 2005, **7**, 3297, DOI: 10.1039/b508541a.

37 Y. Zhao and D. G. Truhlar, A new local density functional for main-group thermochemistry, transition metal bonding, thermochemical kinetics, and noncovalent interactions, *J. Chem. Phys.*, 2006, **125**, 194101, DOI: 10.1063/1.2370993.

38 P. J. Stephens, F. J. Devlin, C. F. Chabalowski and M. J. Frisch, Ab Initio Calculation of Vibrational Absorption and Circular Dichroism Spectra Using Density Functional Force Fields, *J. Phys. Chem.*, 1994, **98**, 11623–11627, DOI: 10.1021/j100096a001.

39 Y. Pang, X. Zhou, E. I. Vovk, C. Guan, S. Li, A. P. van Bavel and Y. Yang, Understanding lanthanum oxide surface structure by DFT simulation of oxygen 1s calibrated binding energy in XPS after in situ treatment, *Appl. Surf. Sci.*, 2021, **548**, 149214, DOI: 10.1016/j.apsusc.2021.149214.

40 B. Jasiewicz, W. Boczoń, T. Borowiak and I. Wolska, Synthesis and structural characterization of zinc(II) acetate complex with α-isosparteine, *J. Mol. Struct.*, 2008, **875**, 152–159, DOI: 10.1016/j.molstruc.2007.04.016.

41 G. Meyer and D. Gieseke-Vollmer, Das wasserfreie Lanthanacetat, $La(CH_3COO)_3$, und sein Precursor, $(NH_4)_3[La(CH_3COO)_6]\cdot 1/2H_2O$: Synthese, Strukturen, thermisches Verhalten, *Z. Anorg. Allg. Chem.*, 1993, **619**, 1603–1608, DOI: 10.1002/zaac.19936190916.

42 A. C. Lazanas and M. I. Prodromidis, Electrochemical Impedance Spectroscopy–A Tutorial, *ACS Meas. Sci. Au*, 2023, **3**, 162–193, DOI: 10.1021/acsmeasuresciau.2c00070.

43 J. P. H. Li, X. Zhou, Y. Pang, L. Zhu, E. I. Vovk, L. Cong, A. P. van Bavel, S. Li and Y. Yang, Understanding of binding energy calibration in XPS of lanthanum oxide by in situ treatment, *Phys. Chem. Chem. Phys.*, 2019, **21**, 22351–22358, DOI: 10.1039/C9CP04187G.

44 Y. Li, D. Li, S. Fan, T. Yang and Q. Zhou, Facile template synthesis of dumbbell-like Mn_2O_3 with oxygen vacancies for efficient degradation of organic pollutants by activating peroxymonosulfate, *Catal. Sci. Technol.*, 2020, **10**, 864–875, DOI: 10.1039/C9CY01849B.

45 M. García-Rodríguez, D. Cazorla-Amorós and E. Morallón, Eco-Friendly Mechanochemical Synthesis of Bifunctional Metal Oxide Electrocatalysts for Zn-Air Batteries, *ChemSusChem*, 2024, e202401055, DOI: 10.1002/cssc.202401055.

46 J. L. Gautier, E. Rios, M. Gracia, J. F. Marco and J. R. Gancedo, Characterisation by X-ray photoelectron spectroscopy of thin $MnxCo_{3-x}O_4(1\geq x\geq 0)$ spinel films prepared by low-temperature spray pyrolysis, *Thin Solid Films*, 1997, **311**, 51–57, DOI: 10.1016/S0040-6090(97)00463-X.

47 M. García-Rodríguez, J. X. Flores-Lasluisa, D. Cazorla-Amorós and E. Morallón, Enhancing Interaction between Lanthanum Manganese Cobalt Oxide and Carbon Black through Different Approaches for Primary Zn–Air Batteries, *Materials*, 2024, **17**, 2309, DOI: 10.3390/ma17102309.

48 J. X. Flores-Lasluisa, M. García-Rodríguez, D. Cazorla-Amorós and E. Morallón, In-situ synthesis of encapsulated N-doped carbon metal oxide nanostructures for Zn-air battery applications, *Carbon*, 2024, **225**, 119147, DOI: 10.1016/j.carbon.2024.119147.

49 S. Chen, Y. Huang, M. Li, P. Sun, X. Lv, B. Li, L. Fang and X. Sun, MnO_x anchored on N and O co-doped carbon nanotubes encapsulated with FeCo alloy as highly efficient bifunctional electrocatalyst for rechargeable Zinc–Air batteries, *J. Electroanal. Chem.*, 2021, **895**, 115513, DOI: 10.1016/j.jelechem.2021.115513.

50 A. K. Friedman, W. Shi, Y. Losovyj, A. R. Siedle and L. A. Baker, Mapping Microscale Chemical Heterogeneity in Nafion Membranes with X-ray Photoelectron Spectroscopy, *J. Electrochem. Soc.*, 2018, **165**, H733–H741, DOI: 10.1149/2.0771811jes.

51 N. A. Merino, B. P. Barbero, P. Eloy and L. E. Cadús, $La_{1-x}Ca_xCoO_3$ perovskite-type oxides: Identification of the surface oxygen species by XPS, *Appl. Surf. Sci.*, 2006, **253**, 1489–1493, DOI: 10.1016/j.apsusc.2006.02.035.

52 N. Han, W. Zhang, W. Guo, H. Pan, B. Jiang, L. Xing, H. Tian, G. Wang, X. Zhang and J. Fransaer, Designing Oxide Catalysts for Oxygen Electrocatalysis: Insights from Mechanism to Application, *Nano–Micro Lett.*, 2023, **15**, 185, DOI: 10.1007/s40820-023-01152-z.

53 A. Morais, J. P. C. Alves, F. A. S. Lima, M. Lira-Cantu and A. F. Nogueira, Enhanced photovoltaic performance of inverted hybrid bulk-heterojunction solar cells using TiO_2/reduced graphene oxide films as electron transport layers, *J. Photonics Energy*, 2015, **5**, 057408, DOI: 10.1117/1.JPE.5.057408.

54 S. Feliu and J. C. Galván, Native Air-Formed Oxide Film and its Effect on Magnesium Alloys Corrosion, *Open Corros. J.*, 2010, **3**, 80–90, DOI: 10.2174/1876503301003010080.

55 J. A. Donadelli, A. Cánneva, G. Erra and A. Calvo, XPS direct analysis on shale rocks: Correlation with kerogen type and maturity, *Fuel*, 2019, **257**, 116004, DOI: 10.1016/j.fuel.2019.116004.

56 P. Chanaud, A. Julbe, P. Vaija, M. Persin and L. Cot, Study of lanthanum-based colloidal sols formation, *J. Mater. Sci.*, 1994, **29**, 4244–4251, DOI: 10.1007/BF00414205.

57 S. Deberdt, S. Castet, J.-L. Dandurand, J.-C. Harrichoury and I. Louiset, Experimental study of $La(OH)_3$ and $Gd(OH)_3$ solubilities (25 to 150 °C), and La–acetate complexing (25 to 80 °C), *Chem. Geol.*, 1998, **151**, 349–372, DOI: 10.1016/S0009-2541(98)00089-8.

58 K. Wang and J. Yu, Lifetime simulation of rechargeable zinc-air battery based on electrode aging, *J. Energy Storage*, 2020, **28**, 101191, DOI: 10.1016/j.est.2019.101191.

59 T. Wang, M. Kunimoto, T. Mori, M. Yanagisawa, J. Niikura, I. Takahashi, M. Morita, T. Abe and T. Homma, Carbonate formation on carbon electrode in rechargeable zinc-air battery revealed by in-situ Raman measurements, *J. Power Sources*, 2022, **533**, 231237, DOI: 10.1016/j.jpowsour.2022.231237.

60 W. Gu, J. Liu, M. Hu, F. Wang and Y. Song, $La_2O_2CO_3$ Encapsulated La_2O_3 Nanoparticles Supported on Carbon as Superior Electrocatalysts for Oxygen Reduction Reaction, *ACS Appl. Mater. Interfaces*, 2015, **7**, 26914–26922, DOI: 10.1021/acsami.5b06100.

61 M. F. Sunding, K. Hadidi, S. Diplas, O. M. Løvvik, T. E. Norby and A. E. Gunnæs, XPS characterisation of in situ treated lanthanum oxide and hydroxide using tailored charge referencing and peak fitting procedures, *J. Electron Spectrosc. Relat. Phenom.*, 2011, **184**, 399–409, DOI: 10.1016/j.elspec.2011.04.002.

62 M. García-Rodríguez, J. X. Flores-Lasluisa, D. Cazorla-Amorós and E. Morallón, Metal oxide Perovskite-Carbon composites as electrocatalysts for zinc-air batteries. Optimization of ball-milling mixing parameters, *J. Colloid Interface Sci.*, 2023, **630**, 269–280, DOI: 10.1016/j.jcis.2022.10.086.

